GSA DATA REPOSITORY 2014371

Probing occurrence of large intra-plate earthquakes at the west flank of the Andes

G. Vargas, Y. Klinger, T.K. Rockwell, S.L. Forman, S. Rebolledo, S. Baize, R. Lacassin, R. Armijo

Supplementary Material

1. Dating Methodology

1.1. Radiocarbon dating

The radiocarbon dating was run on bulk samples. In such case the bulk dates, also termed mean residence time (^{14}C MRT) dates, reflect the average age of disseminated carbon within the sample. The samples are acid-washed to remove secondary carbonate, and treated to eliminate labile organic matter, with the aim to analyze the more resistant organic material.

Conventional radiocarbon results (Table DR1) from bulk organic matter in acidified sediments were calibrated using Calib Radiocarbon Calibration Program (Stuiver and Reimer, 1993), and Intcal09 atmospheric database (Reimer et al., 2009). We report 2σ calibrated age range together with the corresponding heaviest relative probability. Low δ^{13}C values are consistent with C_3 land plants (*e.g.* Meyers et al., 1993), which are abundant in watersheds of the studied area.

Table DR1. Radiocarbon results from organic matter in sediments. Calibrated ages from Stuiver and Reimer (1993) and Reimer et al. (2009).

Sample	Lab. #	δ^{13}C (‰)	Conventional ^{14}C age (yr B.P.)	± (yr)	2σ Cal. age range (yr B.P.; cal. range probability)	Mean Cal. age (yr B.P.)
C01	Beta307135	-24,1	7600	40	8343-8457 (0.98)	8400
C02	Beta307136	-24,1	14030	50	16841-17259 (0.91)	17050
C06	Beta307137	-24,0	15820	60	18779-19328 (1)	19054
C08	Beta307138	-24,9	18240	70	21460-22127 (1)	21794
C09	Beta307139	-24,2	7640	40	8381-8484 (0.85)	8433

References

Meyers, Ph.A., 1997. Organic geochemical proxies of paleoceanographic, paleolimnologic, and paleoclimatic processes. *Organic Geochemistry*, **27** (5/6), 213-250.

Stuiver, M., and Reimer, P. J., 1993, Extended 14C database and revised CALIB radiocarbon calibration program, *Radiocarbon,* **35**, 215-230.

Reimer PJ, Baillie MGL, Bard E, Bayliss A, Beck JW, Blackwell PG, Bronk Ramsey C, Buck CE, Burr GS, Edwards RL, Friedrich M, Grootes PM, Guilderson TP, Hajdas I, Heaton TJ, Hogg AG, Hughen KA, Kaiser KF, Kromer B, McCormac FG, Manning SW, Reimer RW, Richards DA, Southon JR, Talamo S, Turney CSM, van der Plicht J, Weyhenmeyer CE., 2009. IntCal09 and Marine09 radiocarbon age calibration curves, 0–50,000 years cal BP. *Radiocarbon,* **51** (4), 1111–1150.

1.2. Optically Stimulated Luminescence dating

Sediments targeted for optical dating are fine-grained eolian sediments, either loess or silt-rich buried A horizon. Samples for optical dating were taken by hammering a 5 cm interior diameter and 10-15 cm length of copper tubing into profile walls. The outermost 1 cm of sediment inside the tube was removed, leaving an unlight-exposed sediment in the center of the tube for optical dating. Optical ages were determined by two regenerative dose methods on the fine-grained polymineral or quartz fraction. Initially eleven OSL ages were determined on the 4-11, 63-100, 100-150 or the 150-250 μm quartz fractions using a multiple aliquot technique (Jain et al., 2003). Two OSL ages were determined on quartz grains (100-150 μm and 63-100 μm) by single aliquot regeneration protocols. The SAR protocols (Murray, 2003) were selectively applied because most quartz extracts lacked a dominate fast-component and showed appreciable slow and medium components (Murray, 2003). Note that optical ages by the two different techniques overlap at one sigma errors and give added confidence in the resolved chronology.

Multiple aliquot regeneration procedures

Multiple-aliquot regeneration (MAR) procedures with component dose normalization (jain et al., 2003) were used in this study to estimate the equivalent dose on fine-grained polymineral and quartz fraction from sediments (Table DR2). Initially fine grains (4-11 micron) were extracted by suspension settling following Stokes Law and coarse grains (63-100, 100-150 or 150-250 μm) by sieving, after organics and carbonate were removed with soaking in H_20_2 and in HCl, respectively (Aitken, 1998). Quartz extracts on the fine-grained fraction were isolated subsequently by digestion in hydrofluosilicic acid (silica saturated) for six days (Berger et al., 1980; Roberts, 2007). Sediment plate area was approximately circular with a 1 cm diameter. This plate area was used because smaller plate areas are associated with low photon counts, <1000 counts/s at peak emissions for the natural doses. Subsequent ages were only determined with peak emissions of>1000 photon counts/0.4s of the natural and lowest regenerative doses. Low emissions (<200 photon counts/0.4s) at or near the background counts with subsequent infrared excitation indicates a pure quartz separate, as does the presence of 110 ˚C thermoluminescence peak for irradiated aliquots (Koul, 2008). Solar resetting of aliquots prior to MAR analysis was accomplished by 8 hr illumination from a 275W General Electric Mercury

Vapor Sunlamp, removing any pre-existing electrons within accessible photosensitive traps while inducing minimal dose sensitivity changes (Richardson, 1994). Luminescence was measured using a Risø Model TL/luminescence-DA-15 System containing light emitting diodes capable of either infrared (875 ± 30) or blue (470 ± 20) excitation. The resulting luminescence passes through a Hoya U-340 filter (>10% transmission >380 nm) prior to detection within the system's Thorn-EMI 9235 QA photomultiplier tube.

To compensate for laboratory-induced sensitivity changes, we used component specific normalization procedure (Jain et al., 2003). A normalization dose (~4 Gy β) was applied to all discs, either after the measurement of the natural luminescence signal or prior to the measurement of the dose response curve (Table DR2) and the ratio of secondary to initial luminescence response was used to derive a correction factor for sensitivity changes. The efficacy of the preheat treatment (150 °C for 1 hour) for the normalization dose was evaluated by comparing curve shape (trap distribution) between the natural and subsequent dose (Bailey et al., 2003). A similar dose response was indicated by zero or low slope (<0.1) between the luminescence for initial and secondary dose, evaluated at one-second intervals. To eliminate any contributions to the luminescence signal from electrons residing within those traps that are thermally unstable over geologic time periods, two different heating treatments were employed: first, storage at 150°C for 1 hour immediately following each laboratory irradiation (Forman and Pierson, 2002), and second, measurement at elevated temperature 125°C during excitation (Wintle and Murray, 2000). Because the natural luminescence signal does not include any contributions from electrons residing within traps that are thermally unstable over geologic time periods, the first heating treatment is not required prior to its measurement. The temperature and duration of the first heating treatment following the subsequent normalization dose was selected from a range of temperatures (140-200°C) to mimic the charge distribution exhibited by the natural luminescence signal (Fig. DR1). Success was indicated by zero or low slope (<0.1) between the luminescence for initial and secondary dose, evaluated at one-second intervals, and by a uniform equivalent dose value across the shine down curve (Fig. DR1), also indicative of full solar resetting (Bailey et al., 2003). A sequential regenerative dose of up to 255 grays was applied to each sample that exceeded the corresponding natural luminescence and this dose response was unsaturated (Fig. DR2). Equivalent dose was calculated for at least the first 50 seconds of excitation, dependent on background counts, as a weighted mean (Table DR3).

We used laboratory procedures that access the light sensitive luminescence components for quartz components. The most photosensitive traps for quartz are reset within 10 seconds of high-intensity (25mW/cm^2) blue light (470 ± 20nm) exposure (Agersnap-Larsen et al., 2000). These same traps are linked to the 325°C thermal luminescence peak, suggesting that its parent traps are thermally stable over geologic timescales (lifetime >3 x 10^7 years at 20°C) (Wintle and Murray, 2000; Bulur et al., 2000), and are thus suitable targets for luminescence dating studies. This dating study used the blue light emitting diode injection current that was limited to 10% of maximum, minimizing the photo-stimulation intensity and spreading the contributions from the various photosensitive traps over a much longer time period (20 seconds), increasing component resolution. The resulting distributions of the natural luminescence response with increasing photo-stimulation time for these sediments suggested full solar resetting, with a preheat treatment of 150°C for 1 hour yielding a luminescence distribution most similar to the natural emissions (Fig. DR1).

Single aliquot regeneration protocols

Single aliquot regeneration (SAR) protocols (Murray and Wintle, 2003) were used in optical dating quartz separates (1 cm plate area) (Table DR4). An Automated Risø TL/luminescence-DA-15 system was used for SAR analyses. Blue light excitation (470 ± 20 nm) was from an array of 30 light-emitting diodes that delivers ~15 mW/cm^2 to the sample position at 90% power. A Thorn EMI 9235 QA photomultiplier tube coupled with three 3 mm thick Hoya U-340 detection filters, transmitting between 290 and 370 nm, measured photon emissions. Laboratory irradiations used a calibrated ^{90}Sr/^{90}Y beta source coupled with the Risø Reader. The luminescence emissions for all quartz aliquots showed a clear dominance of a fast component (Murray and Wintle, 2003) with > 95% diminution of luminescence after four seconds of excitation with blue light (Fig. DR2). All SAR emissions were integrated over the first 0.8 s of stimulation out of 40 s of measurement, with background based on emissions for the last 30- to 40-s interval.

A series of experiments was performed to evaluate the effect of preheating at 180°, 200°, 220° and 240°C on thermal transfer of the regenerative signal prior to the application of SAR dating protocols (Murray and Wintle, 2003). These experiments showed no preheat-based sensitivity changes and a preheat temperature of 240°C was used in SAR analyses. A test for dose reproducibility was also performed (Murray and Wintle, 2003) with the initial and final regenerative dose of 6.7 or 21 Gy yielding concordant luminescence response (at 1-sigma error) (Fig. DR2). Calculation of equivalent dose by the single aliquot protocols was straightforward with at least 30 aliquots measured for each equivalent dose determination (Table DR3). Equivalent dose distributions are unimodal (Fig. DR2) and the common age model (Galbraith and Roberts, 2012) was utilized for final equivalent dose calculation. Overdispersion values for samples for samples UIC3146 and UIC3372 of 22 ± 3% and 11 ± 3%, respectively are also indicative of single population grain, reflecting the time since solar resetting (Galbraith and Roberts, 2012).

Dose rate

To render an optical age, the environmental dose rate is needed, which is an estimate of sediment exposure to ionizing radiation from the decay of the U and Th series and ^{40}K, and

cosmic sources during the burial period (Table DR3). The U and Th content of sediment assuming secular equilibrium in the decay series and ^{40}K were determined by inductively coupled plasma-mass spectrometry analyzed by Activation Laboratory LTD, Ontario, Canada. A small cosmic ray component of 0.22 to 0.16 mGy/yr for the indicated depth was included in the estimated dose rate (Prescott and Hutton, 1994). Alpha efficiency values for fine-grained quartz separates for samples UIC3142 and 3162, where calculated following procedures in Aitken and Bowman (1975), with respective values of 0.13 ± 0.01 and 0.14 ± 0.01. Moisture content (by weight) for the dated sediment reflects current values at the trench site.

The dose rate for each sample level in a stratigraphic unit is internally consistent and often overlaps at one standard deviation (see Table DR3). Uranium values are in turn very similar down profile with no depth trends, indicating little to none translocation. Thorium to uranium ratios are highly consistently between 4 and 3 and coherent with an ultimate crustal source (Ahrens, 1995). We contend the radioactive disequilibrium if present is a secondary effect and well within the one sigma error of the associated age.

References

Agersnap-Larsen, N., E. Bulur, S. W. S. McKeever, 2000, *Rad. Meas* 32(5-6), 419-425.

Ahrens, T.J., 1995, Global Earth Physics, A Handbook of Physical Constants, AGU Reference Shelf 1, 376 pp.M. J. Aitken, S.G. E. Bowman. *Archaeometry* **17,** 132, 1975.

Aitken, M. J., 1998, *An Introduction to Optical Dating: The dating of Quaternary Sediments by the use of Photon-stimulated luminescence*: New York, Oxford University Press, 267 p.

Bailey, R. M., J. S. Singarayer, S. Ward and S. Stokes, 2003, *Rad. Meas.* **37**, 511.

Banerjee, D., A.S. Murray, L. Botter-Jensen, L. and A. Lang, 2001, *Rad. Meas.* **33(1)**, 73.

Berger, G. W., P. J. Mulhern and D. H. Huntley, 1980, *Ancient TL* **18**, 7.

Bulur, E., L. Bøtter-Jensen and A. S. Murray, 2000, *Rad. Meas.* **32 (5-6)**, 407.

Forman, S. L. and J. Pierson, 2002, *Palaeogeog. Palaeoclimat. Palaeoecol*. **186**, 25.

Galbraith, R. F., R.G. Roberts, G. M. Laslett, H. Yoshida and J. M. Olley, 1999, *Archaeometry* **41**, 339.

Galbraith, R. G. and Roberts, R.G., 2012, *Quaternary Geochronology* **11**, 1.

Jain, M., L. Botter-Jensen, A. K. and Singhvi, 2003, *Rad. Meas*. **37,** 67.

Koul, D. K., 2008, *Pramana – Journal of Physics*, **71**, 1209.

Murray, A. S. and A. G. Wintle, 2003, *Rad. Meas*. **37,** 377.

Prescott, J. R. and J. T. Hutton, 1994, *Rad. Meas.* **23**, 497.

Richardson, C. A, 1994, *Rad. Meas*, **23**, 587.

Roberts, H. M., 2007, *Rad. Meas*. **42**, 1627.

Roberts, H. M., A. G. Wintle, B. A. Maher and M.Y. Hu, 2001, *Holocene* **11,** 477.

Singarayer, J. S. and R. M. Bailey, 2003, *Rad. Meas*. **37(4-5)** 451-458.

Wintle, A. G. and A. S. Murray, 2000, *Rad. Meas.* **32**, 387.

Wood, J.R., S. L. Forman, J. Pierson and J. Gomez, 2010, *Quat. Res*. **73**, 374.

Table DR2. Multiple Aliquot Regenerative Dose Procedure.

Growth Curve	Natural
1. Optical bleaching 8 hr sunlamp	1. Stimulation with blue light and data collection
2. Test dose 4 grays	2. Optical bleaching 8 hr sunlamp
3. Preheat 150° C for 1 hr	3. Test dose 4 Gy
4. Stimulation with blue light and data collection	4. Preheat 150° C for 1 hr
5. Optical bleaching 8 hr sunlamp	5. Stimulation with blue light and data collection
6. Regenerative doses (up to 265 grays)	
7. Preheat 150° C for 1 h	
8. Stimulation with blue light and data collection	

Table DR3: Optically stimulated luminescence (OSL) ages and associated data for offset sediments San Ramon Fault, Chile

Field Number	Laboratory Number	Fraction (microns)/ aliquots	Method and minerology[a]	Equivalent dose (Grays)	U (ppm)[b]	Th (ppm)[b]	K (%)[b]	Alpha efficiency value[c] / (overdispersion)[d]	Cosmic dose (Grays/ka)[e]	Dose rate (Grays/ka)[f]	OSL age (yr)[g]
OSL 5	UIC3162	4-11	MAR, quartz	20.45 ± 1.23	1.0± 0.1	3.2 ± 0.1	0.87 ± 0.01	0.14 ± 0.01	0.20 ± 0.02	2.25 ± 0.13	9080 ± 590
OSL 14	UIC3364	63-100	MAR, quartz	39.48 ± 2.45	1.8 ± 0.1	6.2 ±0.1	1.57 ± 0.02	N/A	0.18 ±0.02	2.28 ± 0.11	17,270 ± 975
OSL 17	UIC3368	63-100	MAR, quartz	41.26 ± 2.68	1.6 ± 0.1	5.9 ± 0.1	1.24 ± 0.02	N/A	0.12 ± 0.01	2.10 ± 0.10	19,630 ± 1120
OSL 24	UIC3365	100-150	MAR, quartz	17.90 ± 1.16	1.6 ± 0.1	5.9 ± 0.1	1.29 ± 0.01	N/A	0.16 ± 0.02	2.12 ± 0.10	8430 ± 480
OSL 24A	UIC3375	63-100	MAR, quartz	41.89 ± 2.70	1.6 ± 0.1	5.7 ± 0.1	1.24 ± 0.01	N/A	0.18 ± 0.02	2.14 ± 0.10	19,530 ± 1095
OSL 26B	UIC3373	63-100	MAR, quartz	39.08 ± 2.40	0.8 ± 0.1	3.0 ± 0.1	1.30 ± 0.01	N/A	0.18 ± 0.02	1.81 ± 0.09	21,580 ± 1370
OSL 27	UIC3372	63-100	MAR, quartz	28.56 ± 1.67	3.4± 0.1	12.2 ± 0.1	1.33 ± 0.01	N/A	0.16 ± 0.02	3.12 ± 0.15	9140 ± 470
OSL27	UIC3372SAR	63-100/29	SAR. quartz	28.59 ± 1.19	3.4± 0.1	12.2 ± 0.1	1.33 ± 0.01	(11 ± 2)	0.16 ± 0.02	3.12 ± 0.15	9155 ± 605
OSL 25A	UIC3374	63-100	MAR, quartz	42.21 ± 2.75	1.6 ± 0.1	5.8 ± 0.1	1.45 ± 0.01	N/A	0.18 ± 0.02	2.12 ± 0.10	19,880 ± 1110

[a]MAR= Multiple aliquot regenerative dose (Jain et al., 2003); SAR =Single aliquot regenerative dose (Murray and Wintle 2003) under blue light (Bl) excitation (470 ± 20 nm).

[b]U, Th and K content determined by ICP-MS by Activation Laboratory Inc. Ontario, Canada.

[c]Alpha efficiency value calculated from Aitken and Bowman (1975)

[d] Values reflects precision beyond instrumental errors; values of ≤ 20% (at 2 sigma limits) indicate low spread in equivalent dose values and an unimodal distribution

[e]From Prescott and Hutton (1994).

[f]Includes a moisture content estimate of 5 ± 2%.

[g]All ages are calculated from the datum year AD 2000 and errors include systematic and random errors.

Table DR4. Single Aliquot Regeneration Protocols for Optical Dating.

Step	Treatment
1	Natural dose or give beta dose
2	Preheat (240º C for 10s)
3	Stimulate with blue light (470 nm) for 40s at 125º C
4	Give beta test dose (e.g. 0.5 Gray)
5	Preheat as in step 2
6	Stimulate with blue light (470 nm) for 40s at 125º C
7	Stimulate with blue light for 40s at 260º C
8	Return to step 1

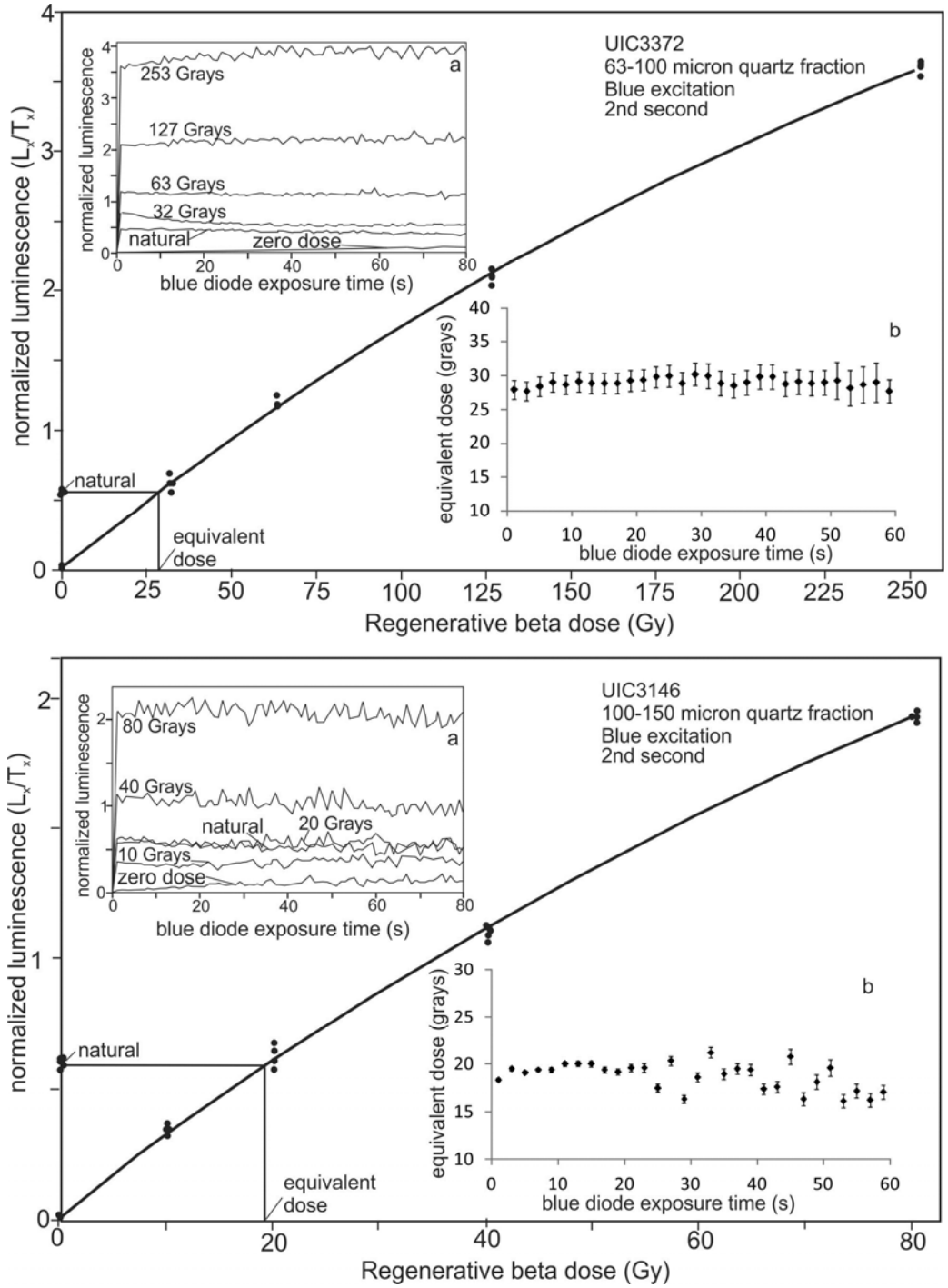

Figure DR1. Multiple aliquot regenerative (MAR) dose response curve for samples UIC3372 and UIC3146 on eolian particles Inset figures (a) show natural luminescence normalized shine down curves and associated regenerative dose response. Inset figures (b) shows equivalent dose for multiple light exposure times (plateau plot), including after 2 s, which is depicted in the main plot.

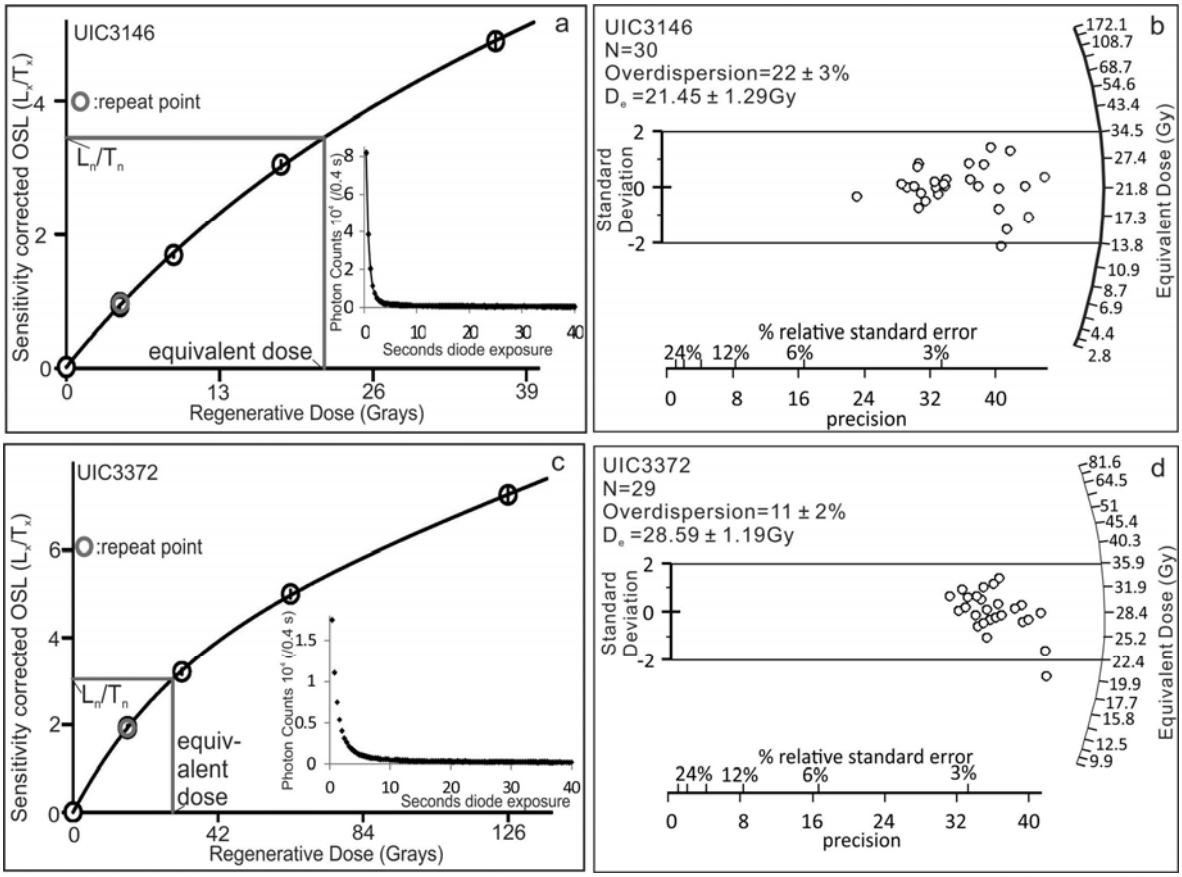

Figure DR2. Luminescence data of quartz aliquots for samples UIC3146 (a and b) and 3372 (c and d). Subfigures a and c show regenerative dose response curve with inset figures show representative photon decay curves for the natural with exposure to blue light from diodes (470 +/- 20 nm). Subfigures b and d are radial plots of equivalent dose data as in lines indicates 2 sigma limits.

1.3. Soil profile description

Description of soil profiles #1 and #2 (Table DR5)

Profile #1 exhibits stronger expression of soil development, with a moderately developed argillic horizon with many secondary clay films, well developed structure but no significant reddening. A 35-40 cm thick layer of the colluvium now comprises the topsoil (A) horizon of the profile, with the relic A horizon now being overprinted with accumulation of secondary clay (BA horizon). The BA horizon is interpreted to reflect development of the argillic horizon up into a relic A horizon due to thickening of the soil by burial of fault-related colluvium. The presence of common secondary clay films in the BA horizon indicates that the distal portion of the colluvial wedge at pedon 1 has been stable for a significant length of time, probably at least several thousand years. The soil extended to below the base of the trench exposure at 1.5 m depth, so it is not known if secondary carbonate is present at this pedon, but there has certainly been sufficient annual moisture to translocate clay to the base of the exposure.

The soil at pedon 2 exhibits similar expression as at pedon 1, but with slightly less development. The argillic horizon is of similar thickness but with only common clay film development and slightly less color. The Ba horizon extends to a total depth of about 140 cm below the surface, with secondary calcium carbonate present as very thin dendritic filaments on the bases of clasts below 175 cm. The presence of a moderately developed argillic horizon associated with pedon 2 indicates that the surface has been relatively stable for many thousands of years. We could find no other evidence for significant surface exposure associated with any of the other buried strata, other than that units V and VII probably reflect some period of time that is needed to accumulate an eolian deposit. Nevertheless, there is no evidence of any B horizon development below the buried A horizons, indicating that the eolian component accumulated fairly rapidly.

Table DR5. Soil descriptions for two pedons in trench 1, north wall.

Pedon	Horizon	Depth (cm)	Description
Profile 1 (at west end of trench)	A	0-37	Dark brown (10YR3/2m, 5/3d); slightly gravelly loam; moderate coarse subangular blocky structure; hard dry consistence, sticky and slightly plastic wet consistence; clear, smooth boundary to:
	BA	37-53	Dark Brown (10YR4/3m, 5/3d); gravelly clay loam; moderate coarse subangular blocky structure; very hard dry consistence, sticky and plastic wet consistence; common thin clay films on clasts and in pores, few thin clay films on ped faces; clear, smooth boundary to:
	Bt1	53-87	Yellowish Brown (10YR 4/4m, 5/3d); gravelly sandy clay loam; strong, fine angular blocky to subangular blocky structure; firm when moist, very sticky and plastic to very plastic when wet; many thin and common moderately thick clay films on ped faces, continuous thick and many thin to moderately thick clay films in pores; gradual, smooth boundary to:
	Bt2	87-117	Yellowish Brown (10YR 4/4m, 5/3d); gravelly sandy loam to loam; moderate medium subangular blocky structure; hard when dry, sticky and slightly plastic to plastic when wet; many thin to moderately thick clay films on clast/matric interfaces, many moderately thick to thick clay films lining pores, common thin to thick clay films on ped faces; gradual, smooth to wavy boundary to:
	BC	117-150+	Yellowish Brown (10YR 4/4m, 5/3d); gravelly sandy loam to loam; weak to moderate, medium subangular blocky structure; slightly hard to hard when dry (although locally extremely hard, suggesting localized cementation), sticky and slightly plastic to plastic when wet; few to common thin clay films on clast/matric interfaces, common thin to moderately thick clay films lining pores, few thin clay films lining ped faces; boundary not observed.

Pedon	Horizon	Depth (cm)	Description
Profile 2 (at 2 m west of fault tip)	A	0-30	Dark brown (10YR3/3m, 5/3d); gravelly silty loam; weak, medium subangular blocky structure; slightly hard dry consistence, non-sticky and non-plastic when wet; no clay films observed; clear to gradual, smooth boundary to:
	Bt	30-75	Yellowish Brown (10YR4/3m); clay loam; moderate, medium subangular blocky structure; hard to very hard dry consistence, sticky and plastic when wet; common to many thin clay films on clast/matric interfaces, common thin and few moderately thick clay films lining ped faces, common thin to moderately thick clay films lining pores; gradual, smooth boundary to:
	BC	75-138	Yellowish Brown (10YR4/4m); sandy loam; weak, medium subangular blocky structure; slightly hard to hard dry consistence, slightly sticky and slightly plastic when wet; common thin clay films lining pores and on clast/matrix interfaces, very few thin clay films on ped faces; gradual, smooth boundary to:
	C	138-175	(color not recorded); sandy loam; massive breaking to weak, coarse subangular blocky structure; slightly hard dry consistence, non-sticky and non-plastic when wet; very few, thin clay films on clast/matric interfaces; abrupt, wavy to smooth boundary to:
	Ck	175-230+	(color not recorded); same as C horizon but with stage I- $CaCO_3$ as dendritic filaments on the bases of clasts.

2. Methodology for Modeling Peak Ground Acceleration in the Basin of Santiago

Seismic motion at near-field distance (<25 km) depends mainly on the earthquake source and rupture propagation characteristics, and on the wave-propagation within the sedimentary basin. The seismic motion can be assessed by modeling earthquake rupture (e.g. Cisternas et al., 2012), while making assumptions on key parameters when they cannot be directly determined in the field. The effects of a sedimentary basin on seismic motion (like in the case of the city of Santiago case, see Pilz et al., 2011) can also be estimated using 3D simulations, although they might rely on (sometimes) poorly constrained hypotheses as well.

Seismic hazard is commonly assessed in engineering applications either using deterministic or probabilistic techniques. The former considers specific scenarios, often chosen among the worst possible scenarios; the latter accounts for the contribution of all the identified earthquake sources weighted by activity rate (i.e. recurrence intervals of earthquakes). Both techniques come out with a similar tool, the response spectrum, which is used by engineers to design the buildings and other facilities.

This spectrum provides the seismic motion variable (e.g. spectral acceleration or velocity) as a function of the frequency of oscillation in Hz. Considering a specific earthquake scenario, the spectrum is commonly estimated in engineering applications with empirical relations based on datasets of seismic motion measurements during historical events at various distances from the earthquake source; these relations are named Ground Motion Prediction Equations (GMPEs). Engineers can, with this input, anticipate the seismic motion associated with an expected event in the natural frequency range of the facility to be designed.

Probabilistic method is the most common application for national hazard assessment for conventional facilities and buildings that constitute the major part of a city like Santiago. In this study, however, we used a deterministic approach, as we want to test the ability of an earthquake on the San Ramón fault to generate seismic motion at virtual sites (depending on the magnitude, distance between site and earthquake source, and local site conditions). We use the recently published Next Generation Attenuation developed for the western USA (NGA-West GMPEs) as they generally apply to crustal earthquakes (Abrahamson et al., 2008). Moreover, they are relevant for our case study because they incorporate the distance between the earthquake fault trace and the site, and not only the epicenter location, and they allow computing models at short distances from the fault. Finally, these attenuation relations are appropriate to address the range of magnitudes (M6 to M8) considered for the San Ramón fault. Among the five NGA-West GMPEs, only four (Abrahamson and Silva, 2008; Boore and Atkinson, 2008; Campbell and Bozorgnia, 2008; Chiou and Youngs, 2008) are here included because they account for the geological site conditions through the mean shear-wave velocity in the 30 first meters (Vs30).

We chose the following characteristics in defining the earthquake scenarios:

- Identical geometrical parameters (dip, depth, width) of the fault are used for all scenarios, derived from Armijo et al. (2010); the surface emergence of the fault rupture –considered in the NGA-west for distance to site assessment- is a direct outcome of the field investigation presented in this paper.

• Thrust fault kinematics is fixed after Armijo et al. (2010) and observations presented in this work.
• 3 possible magnitudes are considered after Pilz et al. (2010) (Mw=6), after Perez et al. (2013) (Mw=6.9) and from our measurements done in the trench (Mw=7.5).
• 2 values of Vs30 (500 and 1000 m/s) are tested that match the low and high bounds of the thick and gravelly deposits lying beneath the city of Santiago (Bonnefoy-Claudet et al., 2008).

Table DR6 presents the results of the sensitivity study (mean values, 1σ uncertainty range not shown). Values and spectra are calculated using the Linda Al Atik spreadsheet available at the following link: http://peer.berkeley.edu/ngawest/nga_models.html

As anticipated, ground motion (PGA) increases with increasing magnitude and decreasing distance. The values reported for the 4 GMPEs are generally consistent and often in the range of standard deviations (not shown here). However, we notice that the PGAs predicted by the CB08 relation are less "magnitude-dependant" than the values computed using the other relations, and that the ground shaking predicted by CY08 is significantly stronger than other explored GMPEs in many cases, especially for large magnitude. The increase in PGA between M6 and M7.5 scenarios is noticeably higher at large distance (10 km). In addition, bad soil conditions (i.e. Vs30=500 m/s) obviously lead to higher PGA values, independently of the distance site-fault source and of the magnitude of the earthquake.

Table DR6. PGA (g) calculated with 4 NGA-west GMPEs (AS08: Abrahamson and Silva, 2008; BA08: Boore and Atkinson, 2008; CB08: Campbell and Bozorgnia, 2008; CY08: Chiou and Youngs, 2008), considering 3 site-to-fault distances (1, 5 and 10 km) and 2 values of shear-velocity in the first 30 meters (Vs30).

PGA (g) d=1 km	AS08		BA08		CB08		CY08		Mean
	Vs=500	Vs=1000	Vs=500	Vs=1000	Vs=500	Vs=1000	Vs=500	Vs=1000	
M6	0.39	0.33	0.38	0.32	0.42	0.38	0.56	0.50	0.41
M6.9	0.50	0.43	0.52	0.44	0.53	0.51	0.68	0.57	0.52
M7.5	0.52	0.46	0.53	0.46	0.53	0.51	0.70	0.61	0.54

PGA (g) d=5 km	AS08		BA08		CB08		CY08		Mean
	Vs=500	Vs=1000	Vs=500	Vs=1000	Vs=500	Vs=1000	Vs=500	Vs=1000	
M6	0.26	0.21	0.22	0.18	0.32	0.28	0.35	0.29	0.26
M6.9	0.37	0.31	0.34	28	0.38	0.34	0.46	0.39	0.36
M7.5	0.41	0.35	0.37	0.32	0.39	0.35	0.53	0.45	0.40

PGA (g) d=10 km	AS08		BA08		CB08		CY08		Mean
	Vs=500	Vs=1000	Vs=500	Vs=1000	Vs=500	Vs=1000	Vs=500	Vs=1000	
M6	0.16	0.12	0.15	0.12	0.21	0.18	0.21	0.17	0.16
M6.9	0.24	0.19	0.25	0.21	0.26	0.23	0.32	0.27	0.24
M7.5	0.29	0.24	0.29	0.24	0.28	0.24	0.39	0.33	0.29

The spectra presented below (Fig. DR3) show the results for the 3 magnitudes, considering the CY08 GMPE, Vs30=500 m/s and distances site-to-fault of 1 and 10 km. It accounts for the whole range of frequencies that are of concern for facilities, buildings or other structures and equipment, typically between several tenths of Hz (e.g. long and tall bridges, skyscrapers) to 5-10 Hz (one or two story buildings), through 0.5-1 Hz for 20-10 story buildings. Note that at short distance (1 km), the 1 g acceleration can be exceeded in the frequency range (2-10 Hz) of concern for industrial facilities.

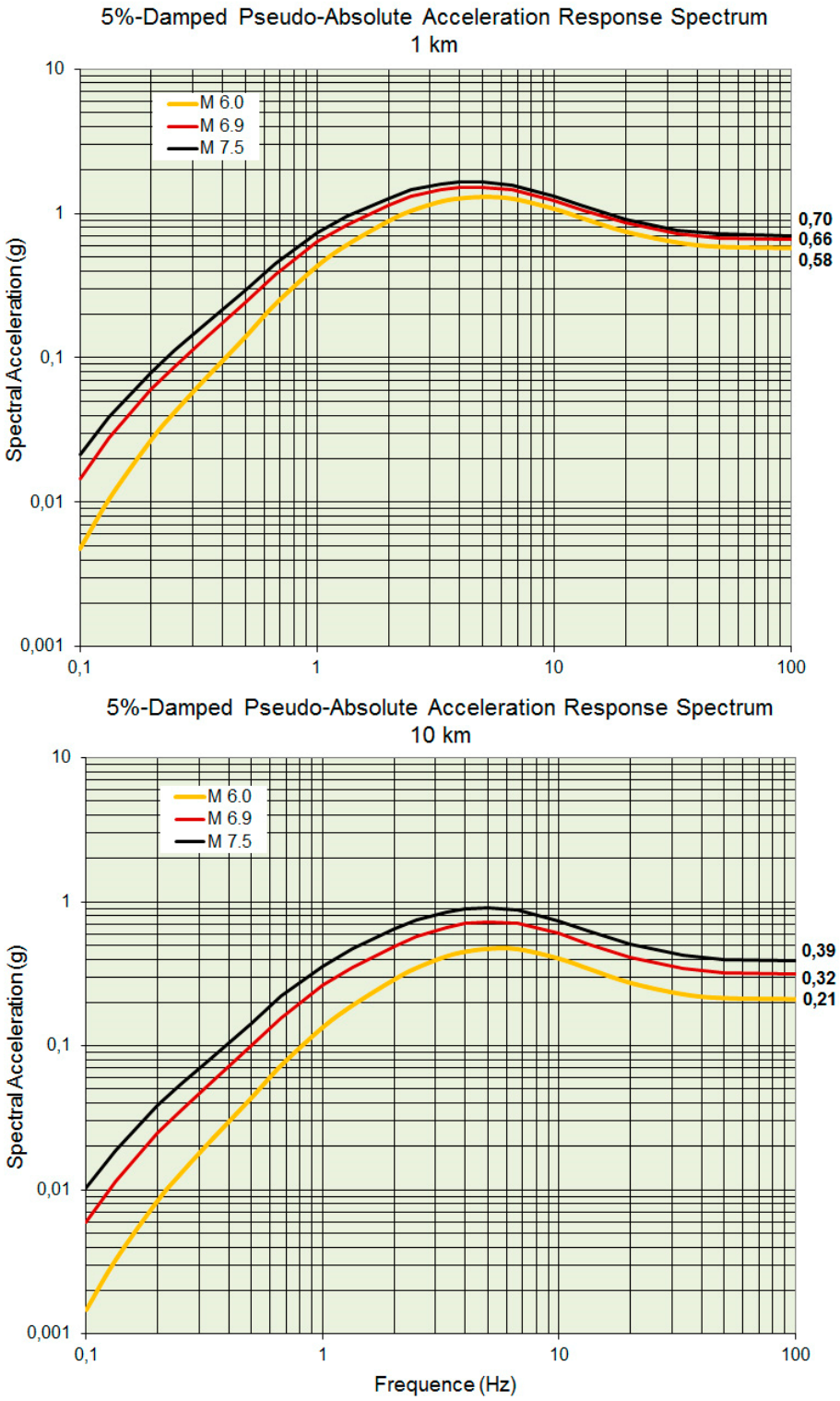

Figure DR3. Response spectra for the 3 magnitude scenarios explored, considering the CY08 GMPE, Vs30=500 m/s and 2 distances site-to-fault of 1 and 10 km.

References

Abrahamson, N. A., Atkinson G., Boore D., Bozorgnia Y., Campbell K., Chiou B., Idriss I. M., Silva W., and Youngs R., 2008, Comparisons of the NGA Ground-Motion Relations. Earthquake Spectra, Volume 24, No. 1, pages 45–66.

Abrahamson, N. A., and Silva, W. J., 2008. Summary of the Abrahamson & Silva NGA groundmotion relations, Earthquake Spectra 24, 67–97.

Armijo R., Rauld R., Thiele R., Vargas G., Campos J., Lacassin R., Kausel E., 2010, The West Andean thrust, the San Ramon and the seismic hazard for Santiago, Chile, Tectonics, 29, TC2007, doi:10.1029/2008TC002427.

Bonnefoy-Claudet S., Baize S., Bonilla L.F., Berge-Thierry C., Pasten C., Campos J., Volant Ph., and Verdugo R., 2008, Site effect evaluation in the basin of Santiago de Chile using ambient noise measurements, Geophys. J. Int., doi: 10.1111/j.1365-246X.2008.04020.x.

Boore, D. M., and Atkinson, G. M., 2008, Ground-motion prediction equations for the average horizontal component of PGA, PGV, and 5%-damped PSA at spectral periods between 0.01 s and 10.0 s, Earthquake Spectra 24, 99–138.

Campbell, K. W., and Bozorgnia, Y., 2008. NGA ground motion model for the geometric mean horizontal component of PGA, PGV, PGD and 5% damped linear elastic response spectra for periods ranging from 0.01 to 10 s, Earthquake Spectra 24, 139–171.

Cisternas, M., Torrejón F., and Gorigoitia N., 2012, Amendingf and complicating Chile's seimic catalog with the Santiago earthquake of 7 August 1580, J. South Am., Earth Sc., 33, 102-109, doi:10.1016/j.jsames.2011.09.002.

Chiou, B. S. J., and Youngs, R. R., 2008. Chiou-Youngs NGA ground motion relations for the geometric mean horizontal component of peak and spectral ground motion parameters, Earthquake Spectra 24, 173–215.

Pilz M., Parolai S., Stupazzini M., Paolucci R., and Zschau J., 2011, Modeling basin effects on earthquake ground motion in the Santiago de Chile basin by a spectral element code, Geophys. J. Int., 187, 929 -945, doi:10.1111/j.1365-246X.2011.05183.x, 2011.

Pérez A., Ruiz J.A., Vargas G., Rauld R., Rebolledo S., and Campos J., 2013, Improving seismotectonics and seismic hazard assessment along the San Ramón fault at the eastern border of Santiago city, Chile. Nat. Hazard, doi:10.1007/s11069-013-0908-3.

3. Additional Figures for Location of the Trench

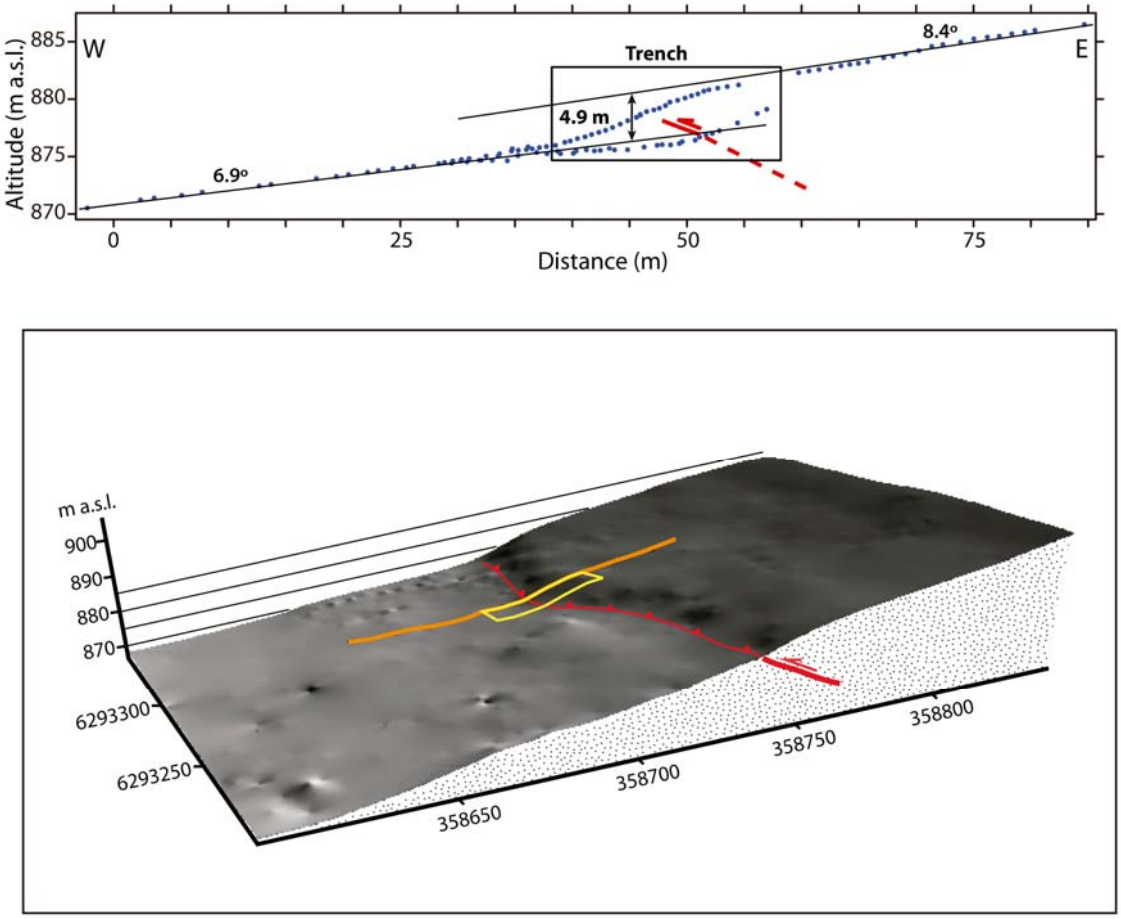

Figure DR4. Scarp topography: Decimetric Digital Elevation Model of the trench site from cinematic GPS survey. The top panel shows the topographic profile corresponding to the orange line. The footprint of the trench is indicated by the yellow rectangle. Irregularities on the lower compartment correspond to meter-size boulders sitting at the surface of the fan. Coordinates are in meters, grid corresponds to UTM 19H.

Figure DR5. Trench view, looking west: The fault scarp makes the topography visible in the foreground of the photography. The wall in the shade is the wall shown in Fig. 2. In the background stands the central part of the city of Santiago de Chile.

4. Earthquake Reconstructions

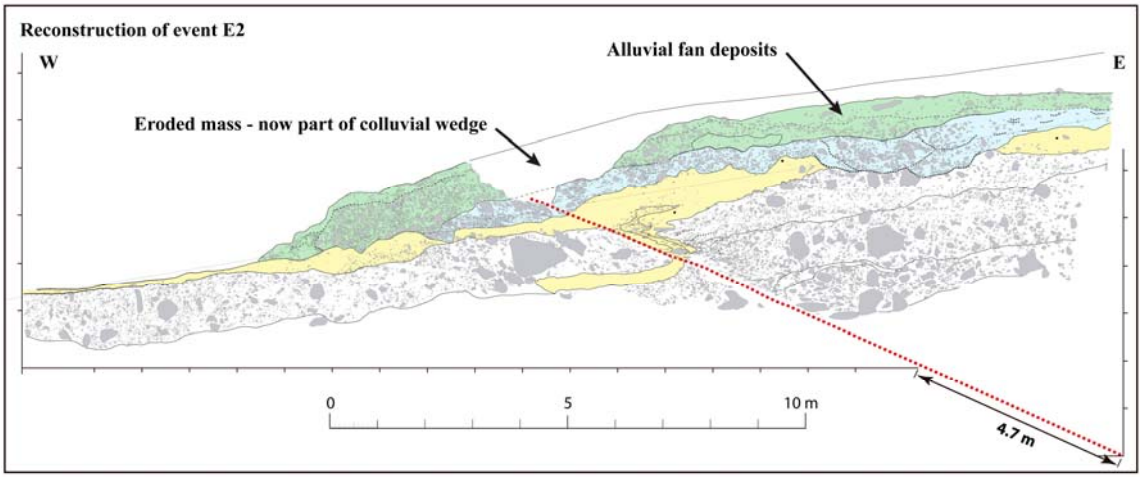

Figure DR6a. Last earthquake reconstruction: Units that pre-date the last event, E2, have been restored to their initial postition by back-slipping the hanging wall such as the corresponding units on each side of the fault get re-aligned. Some units were also unwarped as contact bewteen the different units is expected to be sub-flat. Such reconstruction yields to 4.7 ± 0.2 m of slip during E2. Such reconstructtion evidences the amount of material that was eroded from the hanging-wall to form the colluvial wedge on the foot-wall (not represented here as the colluvial wedge postdates E2). In this reconstruction, the lower unit of eolian sediments in the footwall is still offset, advocating for a penultimate earthquake.

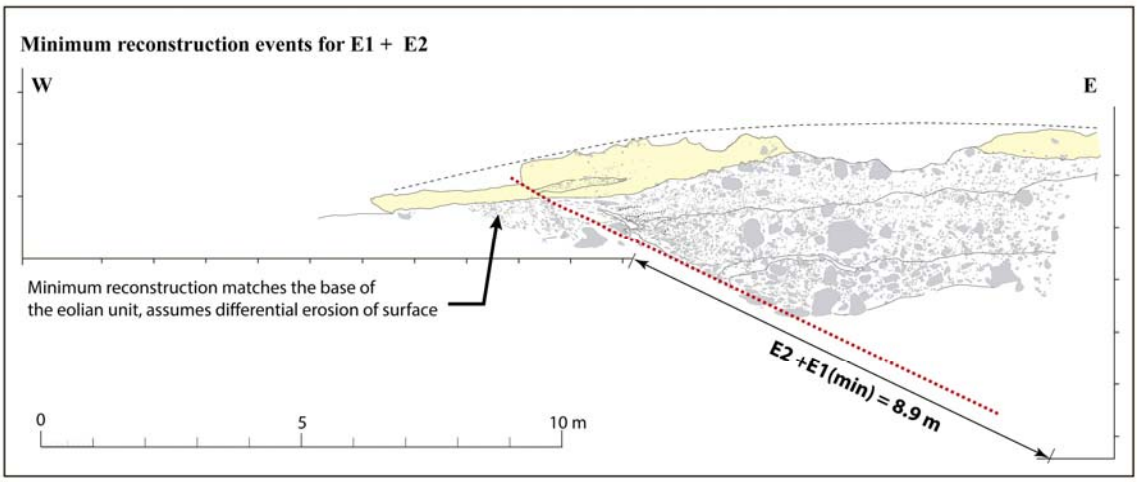

Figure DR6b. Minimum reconstruction for the penultimate event E1: Match of the base of the eolian unit across the fault zone yields a minimum offset of 4.2 m for the penultimate event E1, and a cumulative offset for E2 + E1 of 8.9 m. In such reconstruction some of the units have been unwraped in addition to be moved backward.

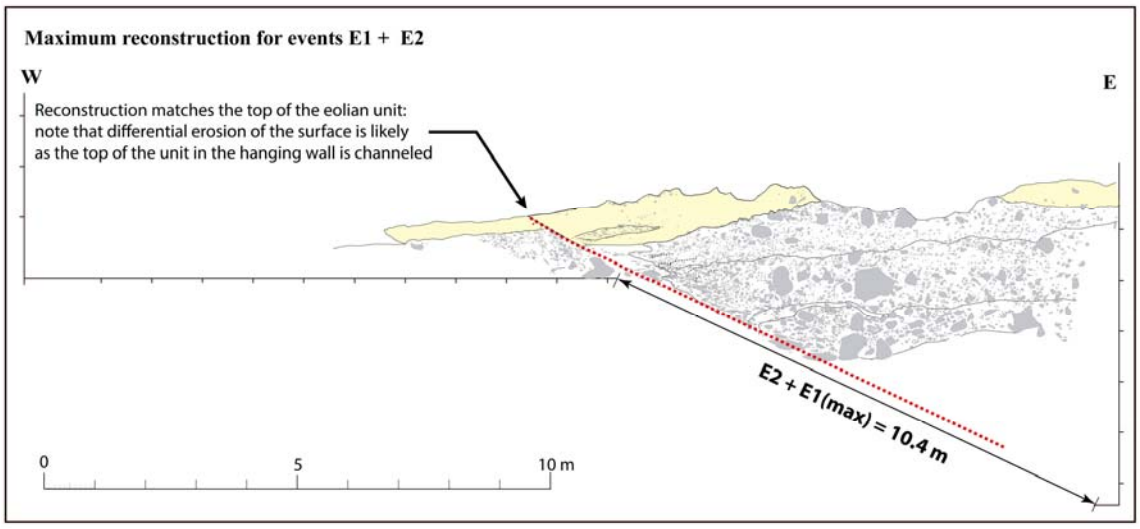

Figure DR6c. Maximum reconstruction for the penultimate event E1: Match of the top of the eolian unit across the fault zone yields to a maximum slip of 5.7 m for the penultimate event E1, and a cumulative offset for E2 + E1 of 10.4 m. Such reconstruction assumes that erosion has been exactly similar on each side of the fault and that in addition to the dip-slip on the fault, some lateral slip also occurs that accounts for the thickness mismatch of the eolian deposit between the two sides of the fault.